Photodiagnosis and Photodynamic Therapy 45 (2024) 103968

Contents lists available at ScienceDirect

Photodiagnosis and Photodynamic Therapy

journal homepage: www.elsevier.com/locate/pdpdt

Investigations on correlations between changes of optical tissue properties and NMR relaxation times

Maximilian Aumiller [a,b,*], Asmerom Arazar [a], Ronald Sroka [a,b], Olaf Dietrich [c], Adrian Rühm [a,b]

[a] Laser-Forschungslabor, LIFE Center, LMU University Hospital, LMU Munich, Planegg 82152, Germany
[b] Department of Urology, LMU University Hospital, LMU Munich, Munich 81377, Germany
[c] Department of Radiology, LMU University Hospital, LMU Munich, Munich 81377, Germany

ARTICLE INFO

Keywords:
Optical properties
Absorption
Scattering
NMR relaxation times
Interstitial photodynamic therapy

ABSTRACT

Background: Accurate light dosimetry is a complex remaining challenge in interstitial photodynamic therapy (iPDT) for malignant gliomas. The light dosimetry should ideally be based on the tissue morphology and the individual optical tissue properties of each tissue type in the target region. First investigations are reported on using NMR information to estimate changes of individual optical tissue properties.
Methods: Porcine brain tissue and optical tissue phantoms were investigated. To the porcine brain, supplements were added to simulate an edema or high blood content. The tissue phantoms were based on agar, Lipoveneous, ink, blood and gadobutrol (Gd-based MRI contrast agent). The concentrations of phantom ingredients and tissue additives are varied to compare concentration-dependent effects on optical and NMR properties. A 3-tesla whole-body MRI system was used to determine T_1 and T_2 relaxation times. Optical tissue properties, i.e., the spectrally resolved absorption and reduced scattering coefficient, were obtained using a single integrating sphere setup. The observed changes of NMR and optical properties were compared to each other.
Results: By adjusting the NMR relaxation times and optical tissue properties of the tissue phantoms to literature values, recipes for human brain tumor, white matter and grey matter tissue phantoms were obtained that mimic these brain tissues simultaneously in both properties. For porcine brain tissue, it was observed that with increasing water concentration in the tissue, both NMR-relaxation times increased, while μ_a decreased and μ_s' increased at 635 nm. The addition of blood to porcine brain samples showed a constant T_1, while T_2 shortened and the absorption coefficient at 635 nm increased.
Conclusions: In this investigation, by changing sample contents, notable changes of both NMR relaxation times and optical tissue properties have been observed and their relations examined. The developed dual NMR/optical tissue phantoms can be used in iPDT research, clinical training and demonstrations.

1. Introduction

Interstitial photodynamic therapy (iPDT) for malignant gliomas [1–3] is currently under development and undergoing clinical trials. For this treatment, a precursor is administered to the patient, which leads to accumulation of a photosensitizer in the target tissue. The photosensitizer is excited by light irradiation and creates reactive oxygen species (ROS) via interaction with intracellular oxygen. In case of 5-aminolevulinic acid (5-ALA) mediated iPDT, the photosensitizer is protoporphyrin IX (PpIX), which is excited at a wavelength of 635 nm. [1,2,4]

As part of the treatment planning, the trajectories for the placement of the light applicators in the brain are defined based on estimates about the light dosimetry [1]. These estimations are based on analytical calculations using diffusion theory under the assumption of homogeneous optical tissue properties [5–7]. In this approximation, the individual optical tissue properties of tumor, white matter, and grey matter are neglected. Currently, more elaborate simulation approaches are under development, using, e.g., Monte Carlo techniques [8]. Here, individual optical tissue properties of different tissue types can be considered and included in the light dosimetry calculations to optimize the light applicator positions in the tissue [8–10].

For the analytical light dosimetry calculations and/or simulations,

* Corresponding author at: Laser-Forschungslabor, LIFE Center, Department of Urology, LMU University Hospital, LMU Munich, Fraunhoferstrasse 20, Planegg 82152, Germany.
E-mail address: max.aumiller@med.uni-muenchen.de (M. Aumiller).

https://doi.org/10.1016/j.pdpdt.2024.103968
Received 31 October 2023; Received in revised form 3 January 2024; Accepted 9 January 2024
Available online 10 January 2024

fixed optical tissue properties may be used, but these properties are actually patient-individual and differ from case to case. In literature, a broad range of optical tissue properties can be found for the same tissue type [11]. This uncertainty can be handled by making worst-case assumptions about the unknown properties or by applying a higher light dose than needed to induce cell death. In case of 5-ALA mediated iPDT, a light overdosage would not affect non-tumor tissue. 5-ALA induced PpIX is mainly selectively accumulating in the tumor tissue and only very low photosensitizer amounts are present in the non tumor tissue [12–14]. Due to destruction of the photosensitizer during the iPDT irradiation (photobleaching process of the photosensitizer), a letal production of ROS is not reached in the non-tumor tissue and healthy tissue is preserved.

Nevertheless, additional tools are desirable that can provide more insight into the patient's individual optical tissue properties. Spectral online monitoring is highly important, as it provides not only insight into the photosensitizer accumulation by measurement of its fluorescence but also into the actual optical conditions by measurement of the treatment light transmission through the tissue [13,15–17]. Using spectral online monitoring (SOM) measurements between two light applicators, one of which emits treatment light while the other one is connected to a spectrometer and used for light detection, it is possible to analytically calculate the optical attenuation in the tissue region between the light applicators and thus within the entire treated tissue volume [5]. Unfortunately, the inhomogeneity of the tissue and the related optical tissue properties had to be neglected so far [18]. A big advantage of SOM is that it provides insight into processes that may alter the optical tissue properties during the ongoing iPDT irradiation. There are indications that oxygenated hemoglobin is actively deoxygenated by iPDT or directly transmuted into methemoglobin [19–21].

Next to the optical light application and monitoring, medical imaging like X-ray computed tomography (CT) and magnetic resonance imaging (MRI) are an essential part of the iPDT procedure. Currently, these are used for therapy planning, guidance, and follow-up disease monitoring. In particular, the target volume of the therapeutic intervention is defined by these imaging modalities [1,22,23].

For the further development of iPDT procedures, light dosimetry and online monitoring, MRI plays an important role. Based on MRI data, different tissue types in the target region can be identified, and individual optical properties can be assigned to them [24,25].

MRI may not only give insight into the localization of different tissue types. The signal intensities visible in MRI are related to the individual relaxation times of the tissues [26]. Important factors influencing the NMR relaxation times in the brain are the lipid content and the free water content of the tissue [27]. The ratio between free and bound water is individual for each tissue and has a strong effect on the differences in the NMR relaxation times between the different tissue types and within the same tissue type.

Next to NMR relaxation in the brain, optical properties are directly related to the water and lipid content of the tissue. In the visible wavelength range, the water content indirectly affects the concentration of the photon absorbing and scattering substances in the sample with higher water content leading to lower optical absorption and scattering. In addition, the optical scattering is related to the lipid content, as lipids are the dominant optical scatterers in biophotonics [28,29].

In addition to lipids, water and blood content also have an influence on optical tissue properties. Furthermore, both are well known to affect the MRI signal intensities, e.g., in edema or hemorrhage, which are related to changes of the NMR relaxation times in the respective regions [30–32].

This leads to the assumption that changes or differences in MRI signal intensities and relaxation times might be an indicator for changes or differences in optical tissue properties in corresponding tissue regions.

To test this assumption, experiments were conducted on optical tissue phantoms with varying compositions and on porcine brain tissues with different amounts of additives by measuring the NMR relaxation times T_1 and T_2 along with the optical absorption and reduced scattering coefficient. Out of this, recipes were created for producing tissue phantoms with MRI relaxation times and optical properties similar to those of different types of brain tissue (white matter, grey matter, malignant glioma) encountered in the target zone during iPDT of malignant brain tumors. First indications for a correspondence of changes in NMR relaxation times and optical properties have been found.

2. Material and methods

2.1. Samples

2.1.1. Dual NMR/optical tissue phantoms

Artificial optical tissue phantoms were used as their properties can be easily adjusted by changing the ingredient concentrations, and they are well known and frequently used in research [33]. Solid homogeneous optical tissue phantoms were manufactured based on agar (Agar, A7002, Sigma-Aldrich, St. Louis, Missouri, USA) and gelatin (Gelatin from porcine skin, G2500, Sigma-Aldrich, St. Louis, Missouri, USA). For adjustment of the optical tissue properties, a 20 % lipid emulsion based on Lipoveneous (Lipovenös® MCT 20 %, Fresenius Kabi Deutschland GmbH, Bad Homburg, Germany) and black ink (brilliant black, no. 4001, Pelikan Holding AG, Schindellegi, Switzerland) were used. To further adjust the T_1 relaxation times of the optical tissue phantoms, gadobutrol, a gadolinium-based contrast agent (GBCA, Gadovist® 1.0 mmol/ml, Bayer AG, Leverkusen, Germany) was added to the artificial tissue phantoms.

To manufacture the tissue phantoms, distilled water was boiled to 95 °C with the corresponding amount of agar. In the case of gelatin, the solution was boiled up to 50 °C. The required amount of Lipoveneous was added in small portions into the solution after it cooled down to 38 °C, where the temperature was kept constant. The temperature of the mixture was controlled with a thermocouple during the process. (In case of Lipoveneous, the pure amount of lipid contained in the 20 % lipid emulsion was used to calculate the Lipoveneous fraction in the phantom.)

After the Lipoveneous was stirred entirely into the solution, the black ink was added to adjust the optical absorbance. If needed, after stirring, the black ink was dissolved in the solution of the GBCA, and both were added to the tissue phantom. Before complete hardening, the tissue phantom was split into two parts. The first part was filled into the cuvette for the integrating sphere measurements (filling quantity 3 ml, CM-A130 2 mm ST, Konica Minolta, Japan). The second part was filled into the cuvette used for MRI measurements.

To reduce edge artefacts in the MRI at the cuvette walls, large volumes cuvetttes (diameter 2.75 mm; filling quantity 50 ml, Sarstedt AG & Co. Kg, Sarstedt Schraubröhre, Nümbrecht, Germany) were used. Occurring edge artifacts in the MRI, usually affect a distance of up to 1.5–1.75 mm distance from the border zone between two tissues or materials [34]. Using the large volumes cuvettes, in the center of the sample a nearly homogeneous signal is obtained, that is not affected by artefacts.

By varying the agar, Lipoveneous and ink fractions, the effects of these ingredients on the optical tissue properties and NMR relaxation times were determined, and suitable compositions to create brain-mimicking tissue phantoms were derived. The finally developed artificial dual NMR/optical phantoms with brain tissue like properties were manufactured four times and measured to investigate their reproducibility in manufacturing.

2.1.2. Porcine tissue samples

Porcine brain was used as tissue samples to compare the effects of additives on optical properties and NMR relaxation times. The porcine tissue was obtained from the butcher. All samples were mixed using a hand blender until a visually homogeneous tissue sample was obtained.

After this mixing process, additional supplements (water, Lipoveneous, or human blood) were added into the tissue sample so that specific additive volume fractions: $c_{additive} = V_{additive}/(V_{tissue} + V_{additive})$ were obtained and the overall volume of the measured sample remained constant.

In case of Lipoveneous, $V_{additive}$ was defined as the volume of the lipid emulsion added to the tissue, not the volume of the pure lipid contained therein. For each supplement concentration, the sample was split and filled into the corresponding cuvettes for the optical and NMR measurements.

The usage of human blood was approved by the Ethics Committee of Ludwig-Maximilians-University, Munich, Germany (reference number 18–144). For the usage of porcine tissues, no ethical approval was required as tissues of animals from the food industry were used.

2.2. MRI measurement and analysis

2.2.1. MRI sample mount and protocol

To determine the T_1 and T_2 relaxation times of the samples, a clinical 3-tesla whole-body MRI system (Magnetom Prisma, Siemens Healthineers AG, Erlangen, Germany) was used. A 32-channel head coil (Siemens Healthineers AG, Erlangen, Germany) was used for all MRI measurements. The samples were positioned in the isocenter of the coil using a self-made sample holder. The sample holder consisted of a box in which the 50 ml sample cuvettes were placed and held in a frame at the bottom and top of the box. The box was filled with water doped with 1 % GBCA to remove artefacts from the surrounding air. The sample holder was placed in the isocenter of the scanner to obtain the best possible sample signals.

To determine parameter maps of the longitudinal relaxation time constant, T_1, a standard inversion recovery half-Fourier-acquired single-shot turbo spin-echo (HASTE) pulse sequence was utilized. This inversion sequence was recorded in 2D slices with single-slice acquisition mode, using a repetition time $T_R = 8420$ ms and an echo time $T_E = 80$ ms. Inversion recovery measurements were performed with 13 different inversion times, T_I, from 50 ms to 8000 ms (50, 150, 250, 500, 750, 1000, 1500, 2000, 3000, 4000, 5000, 6000, 8000 ms). The image resolution of the inversion sequences was $0.6875 \times 0.6875 \times 4.4$ mm^3.

To determine parameter maps of the transverse relaxation time constant, T_2, T_2-weighting HASTE acquisitions with $T_R = 3100$ ms and a total of 20 echo times, T_E, from 25 ms to 500 ms in steps of 25 ms, were used. The image resolution of the T_2-mapping sequences was $0.2083 \times 0.2083 \times 6$ mm^3. The MRI sequences for the determination of T1 and T2 were set in such a way, that the best possible image resolution was achieved to identify inhomogeneities in the samples, while highest possible signal to noise ratio for this resolution is maintained.

For comparison, the finally developed tissue-like dual NMR/optical phantoms were additionally measured with clinical T_1-weighted (T_1 TSE; $T_E = 6.4$ ms; $T_R = 600$ ms; $0.351 \times 0.351 \times 3.6$ mm^3) and T_2-weighted (T_2 TSE; $T_E = 89$ ms; $T_R = 5000$ ms; $0.4688 \times 0.4688 \times 3.3$ mm^3) pulse sequences.

2.2.2. NMR relaxation time evaluation

The image intensities required in the fit procedure were determined from the MRI images using the software ITK-Snap (version 3.8, University of Pennsylvania, Philadelphia, USA) [35]. For this purpose, the sample volume visible in the MRI image in the isocenter of the scanner was segmented manually for each sample (segmentation volumes 5.1 cm^3/~2500 voxels for T1 detemination and 4.9 cm^3/~19,000 voxels for T2 determination). The segmentation was done manually to exclude possible sample inhomogeneities from the following intensity analysis. The mean MRI intensity (I_{mean}) and the standard deviation (I_{STD}) were calculated for each sample based on the segmentation. The MRI T_1-mapping and T_2-mapping sequences were analyzed based on this procedure. Based on the inversion recovery acquisitions, for each T_I, an individual intensity value $I_{mean}(T_I)$ was obtained. Similarly, based on the T_2-mapping acquisitions, mean intensity values $I_{mean}(T_E)$ were obtained.

To determine T_1 from the intensities $I_{mean}(T_I)$, the following model function was used [36,37]:

$$I_{mean}(T_I) = \left| a - b\, e^{\left(-\frac{T_I}{T_1}\right)} \right| \quad (1)$$

Eq. (1) describes a 3-parameter model that is fitted to $I_{mean}(T_I)$ of each sample with free parameters *a, b*, and T_1.

To determine T_2 from the intensities $I_{mean}(T_E)$, the following equation from T_2-relaxometry was utilized [38,39].

$$I_{mean}(T_E) = S_0\, e^{\left(-\frac{T_E}{T_2}\right)} \quad (2)$$

The mono-exponential model curve given by eq. (2) describes the decrease of the spin-echo signal intensity with increasing T_E, depending on T_2 and the proton density signal, S_0, as free fit parameters. The data fitting procedures were implemented in Matlab (Matlab R2018b, MathWorks Inc., Natick, MA, USA). A non-linear least-square model with the iteratively reweighted least squares method was used for the curve fitting procedure, and the individual signal intensities I_{mean} were weighted by their variance calculated from the corresponding I_{STD}. The statistical errors of the obtained values of T_1 and T_2 were derived from the confidence interval (95 %) of the fit.

2.3. Measurement of optical tissue properties

The optical tissue properties of the used samples, i.e. the absorption coefficient $\mu_a(\lambda)$ and the reduced scattering coefficient $\mu_s'(\lambda)$, were characterized using an integrating sphere setup [40]. By measurement of the diffuse reflection and diffuse transmission of the sample, its optical tissue properties were determined via the inverse adding doubling (IAD) procedure [41].

The sample cuvette containing the sample was placed in front of one port (port diameter 25.5 mm) of the integrating sphere (sphere diameter 101.6 mm, Labsphere, North Sutton, USA) and irradiated with a collimated light beam of a xenon arc lamp (D-light 201,332 20, Karl Storz, Tuttlingen, Germany). The spectral data were collected with a detection fibre (core diameter 400 µm, NA: 0.37) inserted into the integrating sphere through the detection port (diameter 3.2 mm). The detection fibre was connected to a spectrometer (S2000, Ocean Optics/Ocean Insight, Ostfildern, Germany). The spectral measurements consisted of three parts. The first part was the measurement of the diffuse transmission signal, $T_{Sig}(\lambda)$: the sample faced the incident light beam under perpendicular irradiation. The collimated, un-scattered part of the light transmitted through the sample leaves the integrating sphere through the exit port (diameter 25.5 mm) opposite the sample. Only the scattered and finally transmitted light, $T_{Sig}(\lambda)$, was detected, without the unscattered transmitted light. The second part was the measurement of the diffuse reflection signal, $R_{Sig}(\lambda)$: the sphere was turned by 180° compared to the diffuse transmission, so only the light scattered and finally reflected by the sample, $R_{Sig}(\lambda)$, was recorded, without the unscattered reflected light. The last part was the recording of the reference signal of the light source, $Ref_{Sig}(\lambda)$, obtained by direct irradiation of the inner surface of the integrating sphere.

From these three spectral datasets, the diffuse transmission $T_d(\lambda)$ and the diffuse reflectance $R_d(\lambda)$ of the sample were calculated using the known reflectivity of the integrating sphere, $R_{IS}(\lambda)$, with the following formula:

$$T_d(\lambda) = \frac{T_{Sig}(\lambda)}{Ref_{Sig}(\lambda)}\, R_{IS}(\lambda) \quad (3)$$

$$R_d(\lambda) = \frac{R_{Sig}(\lambda)}{Ref_{Sig}(\lambda)} R_{IS}(\lambda) \quad (4)$$

The two spectral datasets calculated by Eqs. (3) and (4) were further evaluated with the IAD procedure [41,42], which allows to iteratively determine the spectrally resolved optical parameters $\mu_a(\lambda)$ and $\mu_s'(\lambda)$ of the artificial sample for the wavelength array from 400 to 700 nm.

The mean and error of the optical tissue properties were determined by three separate measurements and evaluation procedures.

2.4. Reference data from literature

The optical tissue properties as well as the NMR relaxation times of the dual NMR/optical tissue phantoms were compared to the literature values seen in Table 1. The optical tissue properties, used for the comparison, were taken for the wavelength 635 nm [43,44]. The wavelength 635 nm was selected as it corresponds to the treatment wavelength of clinical 5-ALA-based iPDT of malignant brain tumors [4]. The NMR relaxation times were taken from literature providing a range for the relaxation times of the brain tissues white matter and grey matter [45–47]. The T_1 and T_2 relaxation times for malignant glioma have not been explicitly reported in the literature. However, they can be assumed to be equal to or longer than those of white matter, as observed in clinical images of malignant gliomas and the directly surrounding white matter [48].

2.5. Data analysis and statistics

All further data analysis and plotting was performed using Matlab (Matlab R2018b, MathWorks Inc., Natick, MA, USA). No statistical tests were performed.

3. Results

3.1. Dual NMR/optical tissue phantoms

Based on the concentration-dependent measurements shown in Figs. S1 through S5 in the supplement to this article, the finally chosen phantom mixtures were tuned manually to obtain optical coefficients and NMR relaxation times that are, at least for the present study, sufficiently close to the reference values listed in Table 1. Three phantom recipes for artificial dual NMR/optical brain tissue phantoms were created. These tissue phantoms have optical properties (μ_a and μ_s' at 635 nm) and NMR relaxation times (T_1 and T_2 at 3 T) similar to white matter, grey matter, and malignant glioma tissue. Table 2 lists the recipes of the three artificial tissue phantoms and their properties μ_a, μ_s' at 635 nm wavelength, and NMR relaxation times T_1 and T_2 at 3 T. All three phantoms were produced in four separate manufacturing processes to test the reproducibility. To investigate the contrast, the three tissue phantoms were filled into the measurement cuvettes as multi-layered phantoms composed of the three different tissue phantoms (see Fig. 1 for an example).

The experimentally determined mean values of the optical tissue coefficients at 635 nm of the three prepared phantoms (Table 2) were all located within the range of the reference values obtained from the literature (Table 1), except for the mean value μ_s'=5.37 mm^{-1} of the white matter phantom. Here, μ_s' is 11 % smaller than the reference value ($\mu_s'_{ref}$=5.6 mm^{-1}), but the error ranges of these two μ_s' values show a small overlap ([5.6–6.5 mm^{-1}] vs. [4.69–5.78 mm^{-1}]).

The mean value of T_1 measured at 3 T on the grey matter tissue phantom was consistent with the corresponding literature range of T_1 (1122–1763 ms), whereas the mean value of T_2 measured on that tissue phantom was about 20 % higher than the upper boundary of the corresponding literature values. The mean value of T_1 measured on the white matter tissue phantom was 3 % shorter than the corresponding lower boundary of the literature range. In contrast, the mean value of T_2 measured on that tissue phantom was consistent with the corresponding literature range. The mean values of T_1 and T_2 measured in the tumor phantom were 19.4 % and 6.2 %, respectively, larger T_2 than those measured on the white matter phantom.

Reproducibility tests have shown that the optical tissue properties at 635 nm could be reproduced within a maximum deviation of 11 % and the NMR relaxation times within a maximum deviation of 14 % for all three phantoms.

In the representations in Fig. 1, the three different phantom layers can be clearly distinguished when combining the information from both NMR imaging modalities (T_1-weighted and T_2-weighted MRI). In T_1-weighted MRI, the white matter layer and the tumor phantom layer appear brighter than the grey matter due to shorter relaxation time, with the white matter phantom having the highest image intensity of the three phantoms. In the T_2-weighted MRI, shorter relaxation times lead to a lower image intensity. The grey matter phantom layer has the longest T_2 time, resulting in the highest image intensity, leading to the strong contrast visible in the T_2-weighted image in Fig. 1. With similar T_2 times, there is only a minimal difference in image intensity between the white matter and tumor phantom layers.

Table 1
Reference values for optical tissue properties, μa and μs' at 635 nm wavelength, and NMR relaxation times, T_1 and T_2 at 3 T, for different types of brain tissue according to literature. These literature values serve as a reference for comparison with the values experimentally obtained within this study [43–47].

tissue	μ_a [mm^{-1}]	μ_s' [mm^{-1}]	T_1 [ms]	T_2 [ms]
grey matter	0.02 [<0.01–0.03]	1.00 [0.88–1.20]	1342 [1122-1763]	102 [88-132]
white matter	0.08 [0.07–0.09]	6.00 [5.60–7.04]	818 [699-927]	72 [69–84]
malignant glioma	0.02 [0.01–0.06]	2.00 [1.00–5.80]	>818	>72

3.2. Porcine tissue samples

To simulate the effects of edema, a haemorrhage and varying lipid content in tissue, measurements have been performed on porcine brain tissue with different amounts of water, human blood, or Lipoveneous added as an additive to the tissue.

The addition of water to porcine brain tissue showed, with increasing volume fraction c_{water} of added water, a decrease of the optical absorption coefficient μ_a at 635 nm. At the same time, both NMR relaxation times T_1 and T_2 at 3 T were prolonged (see Table 3). The reduced scattering coefficient μ_s' at 635 nm showed no clear tendency for increasing c_{water}. In Figure S6 in the supplement, the complete measured wavelength-dependent arrays of the absorption and the reduced scattering coefficient are shown for the different c_{water} values.

The addition of Lipoveneous to porcine brain tissue showed that the absorption coefficient μ_a at 635 nm decreases while the reduced scattering coefficient μ_s' at 635 nm increases with increasing Lipoveneous volume fractions $c_{Lipoveneous}$ (Table 4). (Figure S7 in the supplement shows the complete measured wavelength-dependent arrays of the absorption and the reduced scattering coefficient for the different values of $c_{Lipoveneous}$.)

The NMR relaxation times T_1 and T_2 at 3 T show a non-neglectable T_1 and T_2 prolongation only for the highest Lipoveneous volume fractions $c_{Lipoveneous}$ of 30 %.

In contrast to Lipoveneous' the addition of blood shows, with higher blood volume fraction, an increase of the absorption coefficient μ_a and a decrease of the reduced scattering coefficient μ_s' at 635 nm. In Figure S8 in the supplement, the wavelength dependence of the absorption and reduced scattering coefficient are shown for the different c_{blood} values.

The transverse NMR relaxation time T_2 shortens with higher c_{blood}, whereas the longitudinal relaxation time T_1 does not show any relevant changes (Table 5).

Table 2
Recipes for three brain tissue phantoms with mean optical tissue properties at 635 nm and mean NMR relaxation times at 3 T similar to 3 different types of brain tissue, based on manual analyses of the data from 4 manufacturing processes shown in Figs. S1 through S5 in the supplement of this article. In brackets, the statistical standard error of the corresponding value is shown, determined by four repetitive manufacturing and measurement cycles.

tissue phantom type	agar [%]	Lipoveneous [%]	black ink [%]	gadobutrol [%]	μ_a [mm^{-1}]	μ_s' [mm^{-1}]	T_1 [ms]	T_2 [ms]
grey matter	1	1.5	0.01	0.01	0.020 (0.001)	1.34 (0.04)	1194 (46)	158 (19)
white matter	2	10.5	0.08	0.0167	0.087 (0.009)	5.36 (0.51)	680 (16)	81 (12)
Malignant glioma	2	3.5	0.01	0.0167	0.022 (0.002)	2.39 (0.22)	812 (39)	86 (6)

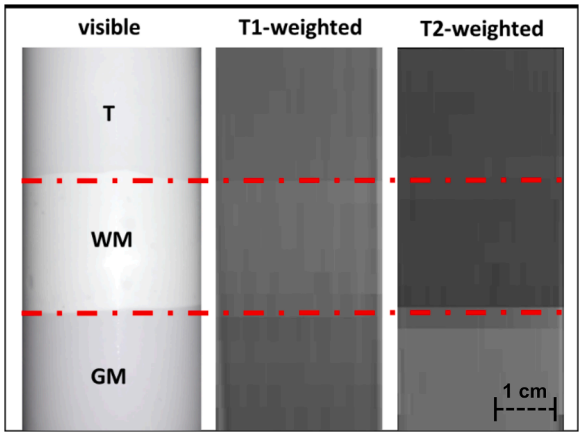

Fig. 1. Visible as well as T_1- and T_2-weighted MRI-appearance of phantoms for mimicking the human brain tissue types malignant glioma/tumor (T), white matter (WM) and grey matter (GM). The red dotdashed lines indicate the interface positions between the different tissue types/phantoms. (The grey value in the NMR images corresponds to the signal intensity in the sample. A shorter T_1 time appears brighter in the T_1-weighted image, while a shorter T_2 time appears darker in the T_2-weighted image [26]).

Table 3
Absorption coefficient μ_a and reduced scattering coefficient μ_s' at 635 nm as well as NMR relaxation times T_1 and T_2 shown for different water volume fractions c_{water}.

c_{water} [%]	μ_a [mm^{-1}]	μ_s' [mm^{-1}]	T_1 [ms]	T_2 [ms]
0	0.069 ± 0.001	3.77 ± 0.05	1119 ± 71	93 ± 7
5	0.069 ± 0.001	4.32 ± 0.08	1181 ± 62	95 ± 5
10	0.064 ± 0.0006	3.84 ± 0.03	1226 ± 40	102 ± 4
15	0.062 ± 0.001	3.95 ± 0.02	1275 ± 57	109 ± 3
20	0.057 ± 0.002	3.62 ± 0.006	1332 ± 75	115 ± 3
30	0.049 ± 0.001	3.27 ± 0.02	1450 ± 74	132 ± 2

Table 4
Absorption coefficient μ_a and reduced scattering coefficient μ_s' at 635 nm as well as NMR relaxation times T_1 and T_2 shown for different Lipoveneous volume fractions $c_{Lipoveneous}$. (Here, the Lipoveneous volume fraction corresponds to the ratio of the volume of the added lipid emulsion and the total volume of the final sample).

$c_{Lipoveneous}$ [%]	μ_a [mm^{-1}]	μ_s' [mm^{-1}]	T_1 [ms]	T_2 [ms]
0	0.068 ± 0.001	4.06 ± 0.10	1124 ± 59	91 ± 6
5	0.065 ± 0.002	4.38 ± 0.09	1106 ± 58	87 ± 6
10	0.067 ± 0.002	4.93 ± 0.08	1114 ± 54	91 ± 6
15	0.066 ± 0.003	5.23 ± 0.04	1123 ± 70	94 ± 5
20	0.068 ± 0.002	5.67 ± 0.10	1132 ± 80	97 ± 5
30	0.052 ± 0.004	6.01 ± 0.04	1226 ± 106	105 ± 5

When comparing the water-induced trends observed on the prepared tissue samples regarding the absorption and the reduced scattering coefficient at 635 nm with those regarding the NMR relaxation times T_1 and T_2 at 3 T, it is observed that a prolongation of relaxation times takes place along with a decrease of absorption and scattering (Fig. 2). An increase of the reduced scattering coefficient at 635 nm by the addition of Lipoveneous was accompanied by a prolongation of T_1 and T_2, when neglecting the sample without added Lipoveneous ($c_{Lipoveneous}$=0 %) (Fig. 3).

Table 5
Absorption coefficient μ_a and reduced scattering coefficient μ_s' at 635 nm as well as NMR relaxation times T_1 and T_2 shown for different blood volume fractions c_{blood}.

c_{blood} [%]	μ_a [mm^{-1}]	μ_s' [mm^{-1}]	T_1 [ms]	T_2 [ms]
0	0.04 ± 0.002	3.95 ± 0.05	1227 ± 100	102 ± 4
2	0.10 ± 0.001	3.92 ± 0.03	1246 ± 55	81 ± 7
4	0.15 ± 0.002	3.90 ± 0.04	1245 ± 127	70 ± 10
6	0.20 ± 0.002	3.86 ± 0.01	1249 ± 125	62 ± 11
8	0.25 ± 0.004	3.69 ± 0.07	1231 ± 119	56 ± 14
10	0.32 ± 0.01	3.74 ± 0.08	1219 ± 102	50 ± 15

Upon adding human blood, an increase of the absorption coefficient at 635 nm and a decrease of the reduced scattering coefficient were accompanied by a shortening of the NMR relaxation time T_2 at 3 T (Fig. 4).

4. Discussion

4.1. Dual NMR/optical brain tissue phantoms

The central ingredient for solid tissue phantoms is the matrix ingredient. For most solid tissue phantoms, hydrogels such as agar, gelatin or nonionic surfactants are used. It was observed that with increasing hydrogel fraction, μ_s', T_1 and T_2 decrease (see Figure S1 and Figure S2 in the supplement to this article). It is well known from the manufacturing of optical tissue phantoms that when increasing the hydrogel concentration, additional scattering medium is needed to maintain a specific scattering power [49]. This is related to the increasing water binding capacity and the decreasing fraction of unbound water within the phantom [50], which is further linked with an increasing storage modulus and stiffness. As a result, it is seen that with increasing hydrogel concentration, T_1 and T_2 are reduced due to the lower fraction of unbound water and decreasing diffusion in the tissue phantom [51].

When comparing agar and gelatin, it was observed that agar had a substantially stronger effect on T_2, which is reduced to 40 ms at 6 % agar, but only to 300 ms at 20 % gelatin (see Figures S1 and S2 in the supplement to this article). For T_1 the effects of agar and gelatin were comparable. The differences between the two hydrogels, e.g. the much higher gelatin fraction required for a given change in NMR relaxation times, may be explained by the different hydrogel mechanisms of agar and gelatin. In agar, the solidification is activated by agarose, a polysaccharide [52]. In contrast, the solidification in gelatin is based on protein chains [53]. In addition, the protein chains are also responsible for the stronger dependence of the resulting phantom properties on the temperature during the manufacturing process [54]. In order to realize the NMR relaxation times T_1 and T_2 in the range 72 - 102 ms listed in Table 1, agar was chosen as matrix for the final tissue phantoms.

Concerning the optical tissue properties, for agar phantoms,

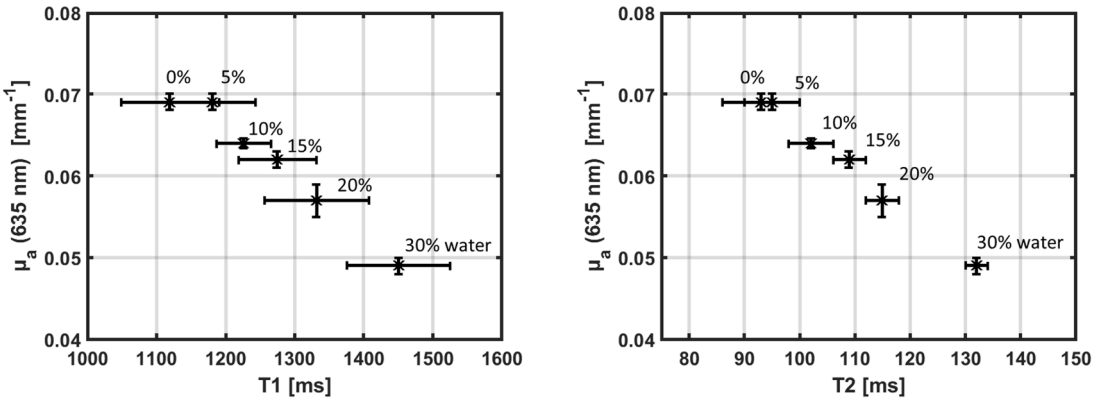

Fig. 2. Absorption coefficient μ_a at 635 nm measured on porcine brain tissue, plotted in relation to the NMR relaxation times T_1 (left) and T_2 (right) for different water volume fractions used to modify the sample properties.

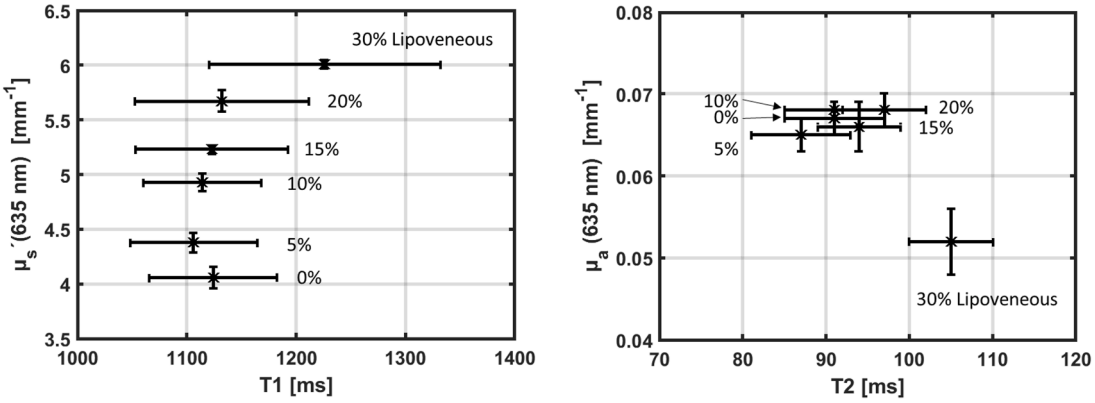

Fig. 3. Absorption coefficient μ_a at 635 nm plotted in relation to the NMR relaxations time T_2 and reduced scattering coefficient μ_s' at 635 nm plotted in relation to the NMR relaxations time T_1, both measured on porcine brain tissue, for different Lipoveneous volume fractions used to modify the sample properties.

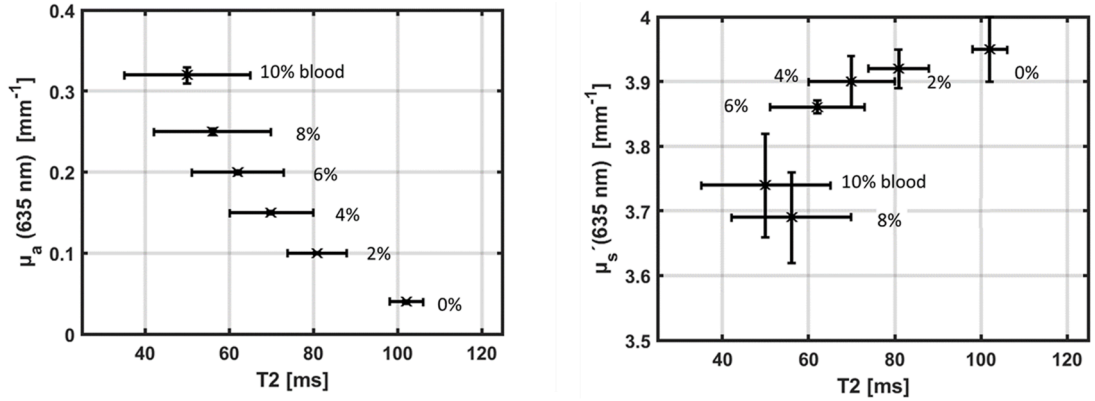

Fig. 4. Absorption coefficient μ_a at 635 nm measured on porcine brain tissue, plotted in relation to the NMR relaxations time T_2 for different human blood volume fractions used to modify the sample properties.

reductions of μ_a were observed when increasing the agar concentration to 4 % and 6 %. At these two concentrations, however, problems in the manufacturing process were observed as the viscosity of the base medium for the tissue phantom is already very high during the cooking process. This problem becomes worse with higher Lipoveneous fractions because the amount of plain water added to the phantom has to be reduced to compensate for the water included in the used 20 % lipid emulsion.

With increasing Lipoveneous fraction in the tissue phantoms, an increase in μ_s' has been observed previously [55]. It is expected that with increasing Lipoveneous fraction, which is comparable to oil and fat, the NMR relaxation times T_1 and T_2 shorten [27,32]. This was only observed to a minor extent in the solid tissue phantoms based on agar or gelatin. Thus, it can be hypothesized that, regarding T_1 and T_2 the influences of the mechanical properties of the hydrogels agar and gelatine dominate over those of dissolved fats and oils, such as Lipoveneous. This reduces the effect of Lipoveneous on T_1 and T_2 when increasing the hydrogel fraction.

Black ink was used to adjust the absorbance in the tissue phantoms. An increasing concentration of black ink resulted in an increase of μ_a,

whereas no systematic changes in μ_s' were observed. As the respective measurements were conducted on a gelatin-based hydrogel, the observed changes of μ_s' could be due to the gelatin itself, since preparation of gelatin-based phantoms is highly sensitive to the exact heating procedure, which can strongly affect the resulting optical properties [54]. No effect on the NMR relaxation times was seen using black ink. As the constituents of black ink are unknown, it is unclear if black ink has no effect at all on the NMR relaxation times or if the effect was not notable due to the low concentration of blank ink in the tissue phantom.

It was possible to reach T_2 values similar to those of human brain with agar-based phantoms, but not with gelatin-based phantoms. To shorten T_1 while keeping T_2 almost constant, gadobutrol, a gadolinium-based contrast agent, was used. In terms of NMR relaxation times, gadobutrol had similar effects on the hydrogel-based phantoms as on tissue. The used gadobutrol concentration was below 0.01 % - 0.0167 %. This corresponds to gadobutrol weight fractions of 0.073 μg/g – 0.123 μg/g within the phantom, which is in the range of values found for gadobutrol accumulation in tumor tissue (0.034 μg/g – 0.627 μg/g) [56].

It has to be noted that the NMR relaxation times T_1 and T_2 of brain tissue observed in individual patients are spread over wide ranges. For the developed tissue phantoms, T_1 and T_2 relaxation times longer than those of white matter were chosen for tumorous tissue, as this is a common finding, but the prologation is dependent on the presence edema, the level of necrosis, and other factors [57,58]. For tumor regions, that have the ability to take up contrast agent, T_1 values in the range of grey matter have been reported.

The obtained tissue phantoms can easily be reproduced, but for easier manufacturing, experience showed that it is helpful to mix the additional ingredients (gadolinium, Lipoveneous and ink) in a separate beaker and add the mixture in small parts into the agar. When adding one ingredient after the other, problems may occur during preparation of the tumor phantom or white matter phantom as the mixture to be processed has a relatively high viscosity.

In the end, recipes for the preparation of dual phantoms mimicking brain tissue with both optical and MR relaxation times close to literature values are presented. In addition, the measurements and results can easily be adapted to create phantom recipes to mimic other tissues, with individually tunable optical and NMR properties. Each of the added ingredients was used to adjust mainly one property of the artificial phantom, without having a significant effect on the other properties. An exception to this is the hydrogel whose concentration defines the basic properties on which the whole tissue phantom is built on, so this is the first component to be chosen, including its concentration. In this case, the agar concentration was used to adjust the T_2 time of the tissue phantom. Afterwards, with Lipoveneous and ink the optical tissue properties can be adjusted. In the end, the needed amount of gadobutrol is added to reduce T_1 to the desired value. Within the relevant concentration range, T_2 was not significantly affected by the addition of gadobutrol.

Of course, one may also use other ingredients to prepare tissue phantoms. For example instead of Lipoveneous other fat-based scattering media like Intralipid and Lipofundin, metal oxides like Titanium dioxide (TiO_2), Barium sulfate ($BaSO_4$) or polysterenes may be used, which are all already being used for manufacturing tissue phantoms [33,54,55,59-61]. For the adjustment of T_1 and T_2, also other metal-based contrast agents may be used [62]. The compatibility between the ingredients has to be tested in each case. Thereafter optical characterization measurements and MRI scans have to be performed to characterize and monitor the different effects on relaxation times and optical properties of the artificial tissue phantom.

Overall, artificial phantoms were developed that simultaneously exhibit optical properties and NMR relaxation times of different types of brain tissues relevant during iPDT. These artificial tissue phantoms may be combined to simulate iPDT a realistic inhomogeneous tissue environment and to investigate and develop simultaneous MRI and spectral online monitoring systems. Furthermore, such artificial phantoms may be used for the development of devices for training and demonstrations.

4.2. Optical properties and NMR relaxation times

In addition to the investigations on artificial tissue phantoms, experiments on porcine brain tissue with different additives were performed to compare their effects on optical properties and NMR relaxation times.

To simulate a tumor-induced edema, water was added to the porcine brain tissue. A brain edema is normally caused by the disruption and leakage of the blood-brain barrier, which causes an accumulation of plasma in the brain parenchyma, which in turn leads to more unbound water in the tissue [58,63]. This causes a prolongation of relaxation times in the edema. This prolongation of T_1 and T_2 was also observed when the water fraction added to the porcine brain tissue was increased. At the same time, a decrease of the absorption coefficient at 635 nm was observed, due to the dilution of tissue constituents strongly absorbing at that wavelength (in particular blood, melanin and lipofuscin). For the reduced scattering coefficient, a systematic decrease was only observed at high water content. The results for the addition of water could indicate that in brain edema surrounding the tumor, the prolongation of relaxation times might be an indicator for a decrease of the absorption coefficient compared to the surrounding tissue not affected by the edema.

Next to the occurrence of edema, it is known that a malignant glioma/glioblastoma also affects the lipid metabolism and the lipid content in the tissue [64,65]. Higher lipid content not only results in a shortening of NMR relaxation times [27,32], it typically also results in an increase of optical scattering [55]. To simulate the reported change of lipid content, Lipoveneous was added to the porcine brain. A shortening of T_1 and T_2 was only seen for 5 % Lipoveneous fraction. With higher fractions, the T_1 and T_2 were prolonged, in contrast to the expectable opposite behaviour just mentioned. This could be because pure Lipoveneous was not available by the manufacturer, but only a diluted 20 % MCT emulsion. Therefore, with the increase of the Lipoveneous fraction, the water fraction in the sample is also increased. This may lead to a domination of the relaxation time prolongation by the higher water content in the sample compared to the effects of the higher lipid content. In conclusion, a systematic increase of optical scattering at 635 nm was observed with increasing Lipoveneous fraction, whereas changes of the optical absorption at that wavelength were negligible and changes of the NMR relaxations times were difficult to interpret. In future experiments, the used Lipoveneous emulsion may be replaced by fat or other lipids without water to simulate changes in lipid content in the tissue more purely.

Next to the tumor-related occurrence of edema or changes in lipid metabolism, the blood content in tissue plays an important role as blood is one of the main optical absorbers in biological tissue [29]. The blood volume in tumor tissue is usually increased due to enhanced angiogenesis. Dependent of the grade of angiogenesis, the relative cerebral blood volume (rCBV) ot tumor, i.e. the ratio of the cerebral blood volume between tumor and white matter, lies in the range 0.82 – 6.26 [66,67]. In some cases, an rCBV higher than 16 was measured [68,69]. To simulate this, blood was added to the porcine brain tissue, which lead to a shortening of T_2 while the absorption at 635 nm increased and T_1 stayed approximately constant with increasing blood fraction. So, in case the changes are blood-related, a shortening of T_2 with constant T_1 in the examined tissue region might be an indicator for higher absorption at 635 nm, which would result in a lower optical penetration depth of the iPDT treatment light.

In addition to T_1 and T_2 mapping to monitor the blood content in the brain, perfusion MRI may give more detailed information as it is sensitive to the cerebral blood flow and volume. Differences in the perfusion may then indicate differences in absorption between the different areas of the brain.

In this investigation, results were presented mainly for 635 nm as this wavelength is used for the 5-ALA-mediated iPDT of malignant gliomas. When using another photosensitizer with a different excitation wavelength, the respective absorption and scattering properties must be expected to change. Depending on the wavelength dependencies of the absorption and scattering coefficients of the investigated base tissue and the additives, the optical coefficients of the modified tissue may change in a different manner at different wavelengths (which not only refers to the magnitude of the change, but also the direction of the change with increasing additive fraction). It has also to be noted that the observed changes will differ for different tissue types such as brain, liver and prostate, depending on the individual water/lipid/blood content of the tissue.

Altogether, a direct translation from T_1 and T_2 values to optical properties is not possible, but for the treatment planning it is already of high value to identify regions with differing optical tissue properties, e.g., higher absorption and scattering. Knowledge about these areas could already be included in the treatment planning and irradiation concept. It could be shown as a first step that changes (or differences) of the NMR relaxation times T_1 and T_2 could indicate changes (or differences) in the absorption and scattering properties.

Future work should also investigate the possibility to extract changes of optical tissue properties with increasing additive fraction based on curve fitting. This may also lead to transfer functions and/or parameters that allow for a translation from changes and differences in T_1 and T_2 relaxation times to temporal changes and local differences in optical properties.

A transfer of MRI to assumptions for differences in optical tissue properties would lead to an individualization of iPDT light dosimetry. This could be implemented in light dosimetry concepts that are able to take into account different tissue types and inhomogeneities with different optical properties in the tissues. By incorporating such individual optical tissue properties, areas that do not receive enough light due to high absorption, for example, can be identified and taken into account in light dosimetry planning. This could ensure the optimal distribution of the light dose at the beginning of the irradiation and possibly lead to a better response of the tumor to the therapy and thus may lead to a longer patient survival.

5. Conclusion

Dual NMR/optical tissue phantoms were designed to mimic simultaneously NMR relaxation times and optical tissue properties of different types of brain tissue. The obtained tissue phantoms can be used not only for iPDT research and development, but also for demonstration and training. In addition, the phantom properties can also be easily adjusted by slight changes of the additive concentrations. By addition of fluorophores, the phantoms could also be further developed to mimic the fluorescence observable during 5-ALA-based iPDT irradiation.

Furthermore, the obtained results from the measurements of porcine tissue samples with addition of water, lipid or blood seem to be a promising first step for further developing iPDT treatment planning concepts based on local differences in optical tissue properties extracted from differences in NMR relaxation times. This possibility is confirmed by the measurements carried out and the indications observed. In future research, these indications should be further investigated so that by using look-up tables or parametrized functions, differences in NMR relaxation times within the same tissue type may be used to identify the grade of change in optical absorption or scattering. This information could be included in the light-dosimetric calculations and the treatment planning to further individualize the iPDT concept.

Institutional review board statement

The study was conducted according to the guidelines of the Declaration of Helsinki and approved by the Ethics Committee of Ludwig-Maximilians-University, Munich, Germany (ref. no. 18–144). For the use of porcine tissue samples ethic approval was not needed as the tissue parts used in this work were all obtained from food production.

Informed consent statement

Informed consent was obtained from all blood donors involved in the study.

Data sharing

Data supporting this study are included within the article and supporting materials.

CRediT authorship contribution statement

Maximilian Aumiller: . **Asmerom Arazar:** Writing – review & editing, Investigation, Formal analysis. **Ronald Sroka:** . **Olaf Dietrich:** Writing – review & editing, Supervision, Methodology, Data curation. **Adrian Rühm:** Writing – review & editing, Validation, Supervision, Software, Project administration, Funding acquisition, Conceptualization.

Declaration of competing interest

The authors declare no conflict of interest. The funders had no role in the design of the study; in the collection, analyses, or interpretation of data; in the writing of the manuscript, or in the decision to publish the results.

Acknowledgments

We thank the Mathias Hübner, Marco Düring and the MRI core facility of the Institute for Stroke and Dementia Research (ISD) at LMU Hospital for their assistance in performing the MRI measurements.

Funding

This research was funded by Deutsche Forschungsgemeinschaft (DFG, German Research Foundation) in terms of the GRK2274 (Project number 299102935). The procurement of the MRI scanner was supported by the DFG grant for major research instrumention (DFG, INST 409/193–1 FUGG).

Supplementary materials

Supplementary material associated with this article can be found, in the online version, at doi:10.1016/j.pdpdt.2024.103968.

References

[1] T.J. Beck, et al., Interstitial photodynamic therapy of nonresectable malignant glioma recurrences using 5-aminolevulinic acid induced protoporphyrin IX (in en), Lasers Surg. Med. 39 (5) (2007) 386–393, 06/2007.
[2] S. Lietke, et al., Interstitial photodynamic therapy using 5-ALA for malignant Glioma recurrences, Cancers 13 (8) (2021). Apr 7.
[3] A. Johansson, F.W. Kreth, W. Stummer, H. Stepp, Interstitial Photodynamic Therapy of Brain Tumors, IEEE J. Selected Topics in Quantum Electronics 16 (4) (2010) 841–853. July 2010.
[4] S. Quach, et al., Interstitial photodynamic therapy for newly diagnosed glioblastoma, J. Neurooncol. 162 (1) (2023) 217–223. Mar.
[5] M. Aumiller, et al., Interrelation between spectral online monitoring and postoperative T1-weighted MRI in interstitial photodynamic therapy of malignant Gliomas, Cancers 14 (1) (2021). Dec 27.
[6] F. Martelli, Light Propagation Through Biological Tissue and Other Diffusive Media: Theory, Solutions, and Software, SPIE Press, 2010, p. 274.
[7] F. Martelli, M. Bassani, L. Alianelli, L. Zangheri, G. Zaccanti, Accuracy of the diffusion equation to describe photon migration through an infinite medium: numerical and experimental investigation (in en), Phys. Med. Biol. 45 (5) (2000) 1359–1373, 2000-05-01.

[8] J. Cassidy, L. Lilge, and V. Betz, "FullMonte: a framework for high-performance Monte Carlo simulation of light through turbid media with complex geometry", 2013, p. 85920H.

[9] E. Oakley, B. Wrazen, D.A. Bellnier, Y. Syed, H. Arshad, G. Shafirstein, A new finite element approach for near real-time simulation of light propagation in locally advanced head and neck tumors, Lasers Surg. Med. 47 (1) (2015) 60–67. Jan.

[10] E. Okada, M. Schweiger, S.R. Arridge, M. Firbank, D.T. Delpy, Experimental validation of Monte Carlo and finite-element methods for the estimation of the optical path length in inhomogeneous tissue, Appl. Opt. 35 (19) (1996) 3362–3371. Jul 1.

[11] V.V. Tuchin, S.o.P.-o.I. Engineers, Tissue Optics: Light Scattering Methods and Instruments for Medical Diagnosis, SPIE Press, 2015.

[12] L. Lilge, B.C. Wilson, Photodynamic therapy of intracranial tissues: a preclinical comparative study of four different photosensitizers, J. Clin. Laser Med. Surg. 16 (2) (1998) 81–91. Apr.

[13] A. Johansson, et al., Protoporphyrin IX fluorescence and photobleaching during interstitial photodynamic therapy of malignant Gliomas for early treatment prognosis: fluorescence for treatment prognosis in Glioma PDT (in en), Lasers Surg. Med. 45 (4) (2013) 225–234, 04/2013.

[14] A. Rühm, et al., 5-ALA based photodynamic management of glioblastoma, in: Proceedings of the SPIE, Optical Techniques in Neurosurgery, Neurophotonics, and Optogenetics, San Francisco, CA, USA, International Society for Optics and Photonics, 2014, 8928p. 89280E.

[15] M. Aumiller, et al., Individualization of interstitial photodynamic therapy for malignant gliomas, in: Medical Laser Applications and Laser-Tissue Interactions IX, 11079, International Society for Optics and Photonics, 2019, 110790P.

[16] A. Johansson, et al., In vivo measurement of parameters of dosimetric importance during interstitial photodynamic therapy of thick skin tumors, J. Biomed. Opt. 11 (3) (2006) 34029. May-Jun.

[17] A. Rühm, et al., 5-ALA based photodynamic management of glioblastoma, in: Proceedings of the Progress in Biomedical Optics and Imaging - Proceedings of SPIE, 2014, 892889280E, 02/28.

[18] L.V. Wang, H.-I. Wu, Biomedical Optics: Principles and Imaging, John Wiley & Sons, 2012, p. 379.

[19] C. Heckl, M. Aumiller, A. Ruhm, R. Sroka, H. Stepp, Fluorescence and treatment light monitoring for interstitial photodynamic therapy, Photochem. Photobiol. 96 (2) (2020) 388–396. Mar.

[20] E.L.P. Larsen, et al., Monitoring of hexyl 5-aminolevulinate-induced photodynamic therapy in rat bladder cancer by optical spectroscopy (in en), J. Biomed. Opt. 13 (4) (2008) 044031, 2008.

[21] E.L.P. Larsen, L.L. Randeberg, O.A. Gederaas, H.E. Krokan, D.R. Hjelme, and L.O. Svaasand, "In vitro study on methemoglobin formation in erythrocytes following hexyl-aminolevulinate induced photodynamic therapy", 2007, p. 642719.

[22] J.E. Villanueva-Meyer, M.C. Mabray, S. Cha, Current clinical brain tumor imaging, Neurosurgery 81 (3) (2017) 397–415. Sep 1.

[23] B. Karakullukcu, et al., MR and CT based treatment planning for mTHPC mediated interstitial photodynamic therapy of head and neck cancer: description of the method, Lasers Surg. Med. 45 (8) (2013) 517–523. Oct.

[24] S.L. Jacques, How tissue optics affect dosimetry of photodynamic therapy, J. Biomed. Opt. 15 (5) (2010), 2010.

[25] Ed B.C. Wilson, M.S. Patterson, S.T. Flock, D.R. Wyman, Tissue optical properties in relation to light propagation models and in vivo dosimetry, in: B. Chance, MA Boston (Eds.), Photon Migration in Tissues, Springer US, 1989, pp. 25–42. Ed.

[26] L. Axel, Relaxation times and NMR signals, Magn. Reson. Imaging 2 (2) (1984) 121–130.

[27] C. Leuze, et al., The separate effects of lipids and proteins on brain MRI contrast revealed through tissue clearing, Neuroimage 156 (2017) 412–422. Aug 1.

[28] W.F. Cheong, S.A. Prahl, A.J. Welch, A review of the optical properties of biological tissues, IEEE J. Quantum Electron 26 (12) (1990) 2166–2185. December 1990.

[29] S.L. Jacques, Optical properties of biological tissues: a review (in en), Phys. Med. Biol. 58 (11) (2013) R37–R61, 2013-06-07.

[30] R. Bansal, X. Hao, F. Liu, D. Xu, J. Liu, B.S. Peterson, The effects of changing water content, relaxation times, and tissue contrast on tissue segmentation and measures of cortical anatomy in MR images, Magn. Reson. Imaging 31 (10) (2013) 1709–1730. Dec.

[31] W.G. Bradley, MR appearance of hemorrhage in the brain (in eng), Radiology 189 (1) (1993) 15–26. Oct 1993.

[32] A. Zimny, L. Zinska, J. Bladowska, M. Neska-Matuszewska, M. Sasiadek, Intracranial lesions with high signal intensity on T1-weighted MR images - review of pathologies, Pol. J. Radiol. 78 (4) (2013) 36–46. Oct.

[33] B.W. Pogue, M.S. Patterson, Review of tissue simulating phantoms for optical spectroscopy, imaging and dosimetry, J. Biomed. Opt. 11 (4) (2006) 041102. Jul-Aug.

[34] M.A. Bernstein, J. Huston 3rd, H.A. Ward, Imaging artifacts at 3.0T, J. Magn. Reson. Imaging 24 (4) (2006) 735–746. Oct.

[35] P.A. Yushkevich, et al., User-guided 3D active contour segmentation of anatomical structures: significantly improved efficiency and reliability, Neuroimage 31 (3) (2006) 1116–1128. July 1, 2006.

[36] A. Karakuzu, et al., qMRLab: quantitative MRI analysis, under one umbrella (in en), J. Open Source Software 5 (53) (2020) 2343, 2020/09/03.

[37] J.K. Barral, E. Gudmundson, N. Stikov, M. Etezadi-Amoli, P. Stoica, D. G. Nishimura, A robust methodology for in vivo T1 mapping, Magn. Reson. Med. 64 (4) (2010) 1057–1067. Oct.

[38] S. Bidhult, G. Kantasis, A.H. Aletras, H. Arheden, E. Heiberg, E. Hedström, Validation of T1 and T2 algorithms for quantitative MRI: performance by a vendor-independent software (in en), BMC Med. Imaging 16 (1) (2016), 12/2016.

[39] D. Milford, N. Rosbach, M. Bendszus, S. Heiland, Mono-Exponential fitting in T2-relaxometry: relevance of offset and first echo, PLoS ONE 10 (12) (2015), 2015-12-17.

[40] M. Eisel, S. Strobl, T. Pongratz, H. Stepp, A. Ruhm, R. Sroka, Investigation of optical properties of dissected and homogenized biological tissue, J. Biomed. Opt. 23 (9) (2018) 1–9. Sep.

[41] S.A. Prahl, M.J.C. van Gemert, A.J. Welch, Determining the optical properties of turbid media by using the adding–doubling method" (in en), Appl. Opt. 32 (4) (1993) 559, 1993-02-01.

[42] S. Prahl, "Optical Property Measurements using the Inverse Adding-Doubling Program", (in en), 2020, p. 53.

[43] T.J. Beck et al., "Clinical Determination of Tissue Optical Properties in vivo by Spatially Resolved Reflectance Measurements", (in en), 2020, p. 10.

[44] A.N. Yaroslavsky, P.C. Schulze, I.V. Yaroslavsky, R. Schober, F. Ulrich, H. J. Schwarzmaier, Optical properties of selected native and coagulated human brain tissues in vitro in the visible and near infrared spectral range (in en), Phys. Med. Biol. 47 (12) (2002) 2059–2073, 2002-6-21.

[45] J.P. Wansapura, S.K. Holland, R.S. Dunn, W.S. Ball, NMR relaxation times in the human brain at 3.0 tesla (in en), J. Magn. Reson. Imaging 9 (4) (1999) 531–538, 04/1999.

[46] H. Lu, L.M. Nagae-Poetscher, X. Golay, D. Lin, M. Pomper, P.C.M. van Zijl, Routine clinical brain MRI sequences for use at 3.0 Tesla (in en), J. Magn. Reson. Imaging 22 (1) (2005) 13–22, 07/2005.

[47] N. Gelman, J.R. Ewing, J.M. Gorell, E.M. Spickler, E.G. Solomon, Interregional variation of longitudinal relaxation rates in human brain at 3.0 T: relation to estimated iron and water contents, Magn. Reson. Med. 45 (1) (2001) 71–79. Jan.

[48] C. Badve, et al., MR fingerprinting of adult brain tumors: initial experience, AJNR Am. J. Neuroradiol. 38 (3) (2017) 492–499. Mar.

[49] R. Cubeddu, A. Pifferi, P. Taroni, A. Torricelli, G. Valentini, A solid tissue phantom for photon migration studies (in en), Phys. Med. Biol. 42 (10) (1997) 1971–1979, 1997-10-01.

[50] C. Wu, W. Ma, Y. Chen, W. Navicha, D. Wu, M. Du, The water holding capacity and storage modulus of chemical cross-linked soy protein gels directly related to aggregates size, LWT 103 (2018), 12/01.

[51] Z.G. Portakal, et al., Design and characterization of tissue-mimicking gel phantoms for diffusion kurtosis imaging, Med. Phys. 45 (6) (2018) 2476–2485. Jun.

[52] M. Nasrollahzadeh, M. Sajjadi, Z. Nezafat, N. Shafiei, Chapter 3 - Polysaccharide biopolymer chemistry. Biopolymer-Based Metal Nanoparticle Chemistry for Sustainable Applications, M. Nasrollahzadeh, Elsevier, 2021, pp. 45–105. Ed.

[53] P. Jaipan, A. Nguyen, R. Narayan, Gelatin-based hydrogels for biomedical applications, MRS Commun. 7 (2017) 416–426, 09/01.

[54] P. Lai, X. Xu, L.V. Wang, Dependence of optical scattering from Intralipid in gelatin-gel based tissue-mimicking phantoms on mixing temperature and time (in en), J. Biomed. Opt. 19 (3) (2014) 035002, 2014-03-06.

[55] R. Michels, F. Foschum, A. Kienle, Optical properties of fat emulsions (in en), Opt. Express 16 (8) (2008) 5907, 2008-04-14.

[56] A. Kiviniemi, M. Gardberg, P. Ek, J. Frantzen, J. Bobacka, H. Minn, Gadolinium retention in gliomas and adjacent normal brain tissue: association with tumor contrast enhancement and linear/macrocyclic agents, Neuroradiology 61 (5) (2019) 535–544. May.

[57] Y. Li, R. Srinivasan, H. Ratiney, Y. Lu, S.M. Chang, S.J. Nelson, Comparison of T(1) and T(2) metabolite relaxation times in glioma and normal brain at 3T, J. Magn. Reson. Imaging 28 (2) (2008) 342–350. Aug.

[58] C.M. Pirkl, et al., Accelerated 3D whole-brain T1, T2, and proton density mapping: feasibility for clinical glioma MR imaging, Neuroradiology 63 (11) (2021) 1831–1851. Nov.

[59] L. Cortese, et al., Liquid phantoms for near-infrared and diffuse correlation spectroscopies with tunable optical and dynamic properties, Biomed. Opt. Express 9 (5) (2018) 2068–2080. May 1,.

[60] M.S. Durkee, L.D. Nash, F. Nooshabadi, J.D. Cirillo, D.J. Maitland, K.C. Maitland, Fabrication and characterization of optical tissue phantoms containing macrostructure, J. Vis. Exp. (132) (2018). Feb 12.

[61] D. Passos, J.C. Hebden, P.N. Pinto, R. Guerra, Tissue phantom for optical diagnostics based on a suspension of microspheres with a fractal size distribution, J. Biomed. Opt. 10 (6) (2005) 064036. Nov-Dec.

[62] Y.D. Xiao, R. Paudel, J. Liu, C. Ma, Z.S. Zhang, S.K. Zhou, MRI contrast agents: classification and application (Review), Int. J. Mol. Med. 38 (5) (2016) 1319–1326. Nov.

[63] Y. Esquenazi, V.P. Lo, K. Lee, Critical care management of cerebral edema in brain tumors, J. Intensive Care Med. 32 (1) (2017) 15–24. Jan.

[64] H. He, et al., Method for lipidomic analysis: p53 expression modulation of sulfatide, ganglioside, and phospholipid composition of U87 MG glioblastoma cells, Anal. Chem. 79 (22) (2007) 8423–8430. Nov 15.

[65] K. Abdul Rashid, K. Ibrahim, J.H.D. Wong, N. Mohd Ramli, Lipid alterations in glioma: a systematic review, Metabolites 12 (12) (Dec 16 2022).

[66] H.J. Aronen, et al., Cerebral blood volume maps of gliomas: comparison with tumor grade and histologic findings (in en), Radiology (1994), 1994-04-01.

[67] S.J. Lee, et al., Perfusion MR imaging in gliomas: comparison with histologic tumor grade, Korean J. Radiol. 2 (1) (2001) 1–7, 2001.

[68] T. Sugahara, et al., Correlation of MR imaging-determined cerebral blood volume maps with histologic and angiographic determination of vascularity of gliomas, AJR Am. J. Roentgenol. 171 (6) (1998) 1479–1486. Dec.

[69] M. Law, et al., High cerebral blood volume in human gliomas predicts deletion of chromosome 1p: preliminary results of molecular studies in gliomas with elevated perfusion, J. Magn. Reson. Imaging 25 (6) (2007) 1113–1119. Jun.